

Coupled Vibrations in a Thermo-Elastic Small Size Scanning Probe Microscopy Array

Dennis Roeser¹⁾, *Stefanie Gutschmidt²⁾, Thomas Sattel³⁾ and Ivo W.
Rangelow⁴⁾

^{1), 3)} *Department of Mechatronics, ⁴⁾ Department of Microelectronic and
Nanoelectronic Systems, Ilmenau University of Technology, Ilmenau, Germany*

²⁾ *Department of Mechanical Engineering, University of Canterbury,
Christchurch, New Zealand*

¹⁾ dennis.roeser@tu-ilmenau.de

ABSTRACT

In view of increasing the performance of scanning probe microscopy (SPM) cantilever arrays could outperform current single cantilever systems with respect to scan rates. However, challenges to date are to comprehend the coupled dynamics of the system in close proximity to a sample surface and to developed advanced control schemes. To meet these challenges, we contribute a new mathematical model, capturing the mechanical response, thermal actuation as well as near-field force mechanisms.

The theoretical work is motivated by experimental investigation of our PRONANO array. The governing equations of the array, derived in this work, are a set of coupled partial differential equations based on Euler-Bernoulli beam theory and on a Fourier's heat conduction model, with an excitation model derived from Joule heating. The coupling between each resonator in the array is considered as a set of discrete spring and damping elements.

A first analysis of the derived model is focused on the modal behavior of the system, which shows the coupled eigenmodes of the array as well as localized intrinsic modes in dependence of critical parameters like e.g. effective distances between the microbeams. The results are compared with a finite element model in order to validate the coupling and boundary conditions.

1. INTRODUCTION

Scanning probe microscopy (SPM) is a process to acquire three dimensional images with a sub-nanometer resolution [1-3]. The development and advances of SPM technology have been reported by e.g. Giessibl [1] and Wiesendanger [2, 3]. Due to the scan motion and the dynamics of the probe itself, the time needed to acquire an image is high, especially in cases of large scan areas (e.g. from 100 μm to 1 mm). Among others, arrays promise an innovative solution to this challenge by using parallelized probes which operated over a certain area of the sample surface simultaneously. Thus, each resonator has a comparably small area to scan, which significantly shortens the

overall scan process [4]. Furthermore, this technology also opens the possibility to simultaneously image and manipulate the sample. Despite obvious advantages of arrays in SPM application, the technology yields the need for integrated actuation and displacement sensing for each element of the array. Further miniaturization and a decreasing of distance between single resonators of an array are also desirable. This implies a more complex system, consisting of multiple coupled physical fields (e.g. depending on the principle of actuation; thermo-mechanical, electrostatic-mechanical etc.) as well as an elastic coupling between the resonators. The control effort to achieve high scan rates with a high spatial resolution increases due to the need to control each resonator individually. In order to understand the overall behavior as well as to develop new control schemes to meet increasing demands on precision and performance, a mathematical model is indispensable. In this work an analytical, multi-physics model of the PRONANO array [5] is derived to set the basis for a systematic nonlinear dynamics analysis (see Fig. 1).

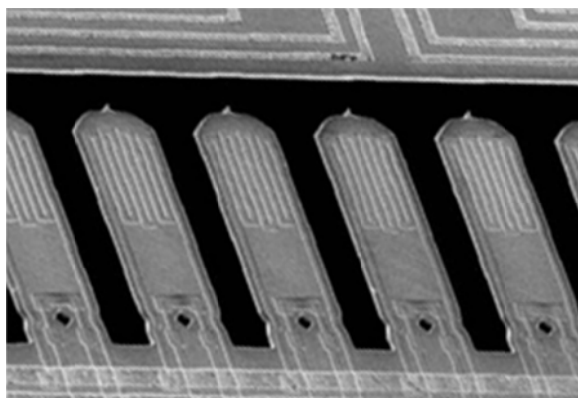


Figure 1: Photograph of the coupled microbeam PRONANO array with meander shape actuator and piezoresistive sensor, located close to the common base [6]

1.1. Thermally actuated micro-cantilevers

A single, thermal actuated microbeam (as well as the whole array) is based on CMOS fabrication technology [7]. The micro-cantilever is a Silicon (Si) beam with integrated piezoresistive readout and thermal actuation and its motion is generated by means of the bi-morph effect. A cross-sectional profile reveals three layers, namely, silicon on insulator, silicon dioxide and an aluminum layer, forming the meander shaped microheater. The piezoresistive sensor is formed within the oxide layer by boron implantation. In view of the beam's composite structure, the corresponding bi-morph effect, as well as of the different cross-sectional areas along the cantilever's length, a multi-regional continuum mechanics approach is chosen to model the single resonator. A detailed derivation of governing equations of the single cantilever is available in Sattel et al. [8]. In this paper, we expand this model to the formulation of a one dimensional array with an arbitrary number of members. A first analysis concentrates on a small-size array (of 4 resonators) and developing realistic boundary conditions and coupling mechanisms for the array.

2. ANALYTICAL MODEL

The derivation of array models, capable of explaining highly non-linear effects [9-13], has shown to be a challenging task, due to the amount of coupled fields, often nonlinear behavior and different scientific domains involved [14-18]. To date, most theoretical approaches for multi-physics structures include only two coupled fields, e.g. electro-mechanical [19-21], thermo-mechanical [22] or piezoelectric-mechanical interactions [23]. In this work we propose a model that includes all actuation, interaction and sensing mechanisms, which concludes in a total of four coupled fields, which are thermal, piezoresistive, mechanical and near-field probe-sample interactions.

2.1. Design and Notation

The array model presented in this work is based on our derivations of the single microbeam model [8] and accounts for the spatio-temporal behavior of the mechanical structure coupled with the thermal actuation mechanism as well as near field probe-sample interactions. Note, that the thermal actuation in our previous work has been modeled by means of a thermal moment, which in this work is replaced by considering the multi-layered profile of the composite structure. Detailed derivations concerning the kinematics and dynamics that yield the actuation model will be published elsewhere. Schematic sketches of the n -th microbeam and the array are depicted in Fig. 2. The coordinate system is located at the clamped end of each microbeam, where

$$0 \leq \tilde{x}_n \leq L_n, -\frac{B_n}{2} \leq y_n \leq \frac{B_n}{2}, -\frac{H_n}{2} \leq z_n \leq \frac{H_n}{2}. \quad (1)$$

The dimensions of the cantilever are the length L_n , the width B_n and the height $H_n = \sum_{i=1}^3 h_i$, respectively (variables denoted with a *tilde* are going to be made non-dimensional below.) The microbeam is a composite structure consisting of three layers, denoted throughout the article with the subscript i , that are: Silicon ($i = 1$), silicon dioxide ($i = 2$) and aluminum ($i = 3$). As can be seen in Fig. 2, each beam has a varying cross-sectional area along its length, due to the meander shape of the aluminum layer. These different sections are denoted by subscript j .

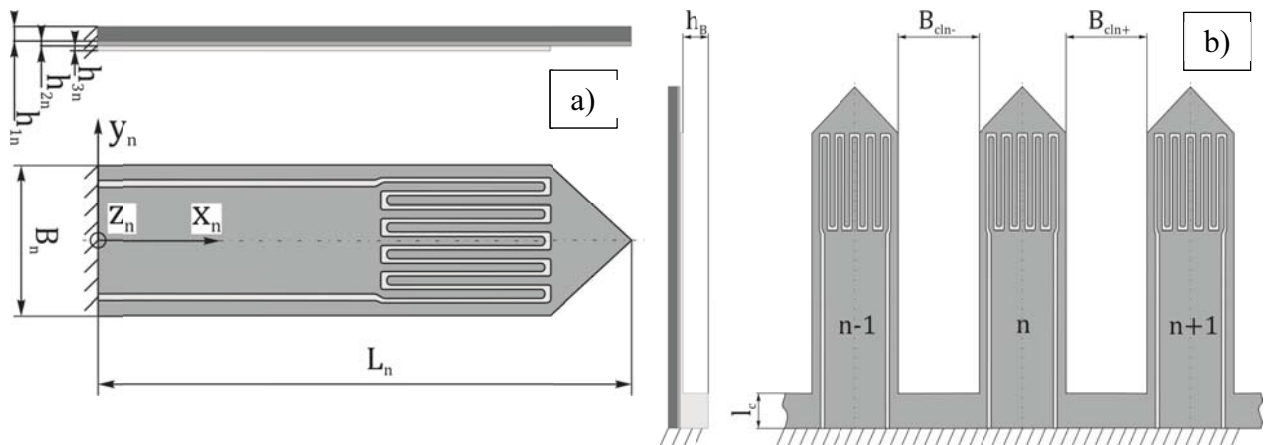


Figure 2: a) Schematic sketch of a single microbeam; b) Microbeam array

The members of the array are mechanically coupled via a common base of the thickness h_B and the corresponding length l_c (see Fig. 2b). The distances between neighboring members are $B_{cln\mp}$ with $n = 1..N$, wherein N is the number of microbeams in the array. The subscript \mp represents either the foregone or the next microbeam in the array. Thus, B_{cln-} is the distance between the microbeam $n - 1$ and n and B_{cln+} the distance between beam n and $n + 1$. Note that the first and last resonators in the array are coupled to a neighboring member on one side and to a fixed structure on the other to allow for equal behavior across the entire system. Definitions and values of the parameters can be found in Appendix A.

2.2. Multi-Physics Continuum Model

We consider the structurally coupled array of N microbeams as depicted in Fig. 2. The governing equations of motion of the n -th resonator are derived using Newton's and Hamilton's principles and is based on the thermoelastic constitutive equation [24], considering the composite structure of the beam, which leads to:

$$\begin{aligned} \frac{\partial^2}{\partial t^2} \tilde{w}_n &= Q_n(\tilde{\theta}_n, \tilde{w}_{n,\tilde{t}}) - R_n(\tilde{w}_n) \\ &+ F_{cdn}(\tilde{w}_{n-1}, \tilde{w}_n, \tilde{w}_{n+1}, \tilde{w}_{n-1,\tilde{t}}, \tilde{w}_{n,\tilde{t}}, \tilde{w}_{n+1,\tilde{t}}) + F_{TSn}(\tilde{w}_n) \\ \frac{\partial}{\partial t} \tilde{\theta}_n &= Q_{HF}(\tilde{\theta}_n) - Q_{CE}(\tilde{w}_{n,t}, \tilde{t}), \end{aligned} \quad (3)$$

with the displacement in z direction \tilde{w}_n and the temperature difference $\tilde{\theta}_n = T_0 - T_n$, wherein T_n is the temperature and T_0 is the initial temperature of the system. Partial derivatives with respect to time or space are also denoted by $(\)_{,\tilde{t}}$ and $(\)_{,\tilde{x}}$.

The mechanical boundary conditions of (3) are

$$\begin{aligned} \tilde{w}_n(0, \tilde{t}) &= 0, \quad \frac{\partial}{\partial \tilde{x}_n} \tilde{w}_n(0, \tilde{t}) = 0, \\ M_n(L_n, \tilde{t}) &= 0, \quad \frac{\partial}{\partial \tilde{x}_n} M_n(L_n, \tilde{t}) = 0, \end{aligned} \quad (4)$$

and represent the most ideal case, which for a single cantilever has provided quantitative results [20, 25]. However, in view of predicting the behavior of the coupled array, these conditions may or may not be true. Thus, this work lays the emphasis on careful investigations of observed coupling phenomena to derive and to validate a realistic set of boundary conditions.

The momentum about the y -axis in (4) is

$$M_n = -(\bar{A}_n \bar{I}_{yn} - \bar{S}_{yn}^2) \frac{E_{n1}}{\bar{A}_n} \frac{\partial^2}{\partial \tilde{x}_n^2} \tilde{w}_n + (\bar{A}_n \bar{\alpha}_n \bar{S}_{yn} - \bar{A}_n \bar{S}_{yn} \bar{\alpha}_n) \frac{E_{n1}}{\bar{A}_n} \tilde{\theta}_n. \quad (5)$$

Coefficients denoted by a bar $(\bar{\ })$ represent the sum of this quantity over the different layers across the beam thickness. Definitions and values of all coefficients can be found in Table 1 in Appendix A. A_n , S_{yn} , I_{yn} , E_{1n} and α_n are the area of cross-section,

the first and second moment of area, the Young's modulus of silicon and the coefficient of thermal expansion, respectively.

The thermal boundary conditions are considered to be isothermal at the clamped end (with $T_n(0, \tilde{t}) = T_0$) and adiabatic at the free end of the microbeam. Thus,

$$\tilde{\theta}_n(0, \tilde{t}) = 0, \quad \frac{\partial}{\partial \tilde{x}_n} \tilde{\theta}_n(L_n, \tilde{t}) = 0. \quad (6)$$

Watanabe et al. [26] verified these boundary conditions by means of FEA simulations as well as in comparison to experimental data.

The restoring force $R_n(\tilde{w}_n)$ in (3) is that of a standard Euler–Bernoulli beam with immovable boundary conditions in case of a composite structure as well as a coordinate system located outside the center of gravity of the overall beam area A_n ,

$$R_n(\tilde{w}_n) = (\bar{A}_n \bar{I}_{yn} - \bar{S}_{yn}^2) \frac{E_{n1}}{\bar{A}_n \mu_n} \frac{\partial^4}{\partial \tilde{x}_n^4} \tilde{w}_n, \quad (7)$$

where μ_n is the beam's density per unit length. The $Q_n(\tilde{\theta}_n, \tilde{w}_n, \tilde{t})$ terms in (3) represent the system's damping mechanisms and consist of a thermal and a viscous part

$$Q_n(\tilde{\theta}_n, \tilde{w}_n, \tilde{t}) = (\bar{A} \bar{\alpha}_n \bar{S}_{yn} - \bar{A} \bar{S}_{yn} \bar{\alpha}_n) \frac{E_{n1}}{\bar{A}_n \mu_n} \frac{\partial^2}{\partial \tilde{x}_n^2} \tilde{\theta}_n - \frac{d_n}{\mu_n} \frac{\partial}{\partial \tilde{t}} \tilde{w}_n, \quad (8)$$

All microbeams share the same base structure (see Figure 1 and 2b), which couples the motions of the individual members. To predict these coupling mechanisms in realistic mathematical expressions we put the emphasis of this paper on the study of boundary conditions and coupling phenomena. Herein, the neighboring elements are connected with discrete spring-damper elements, as depicted in Figure 3. The

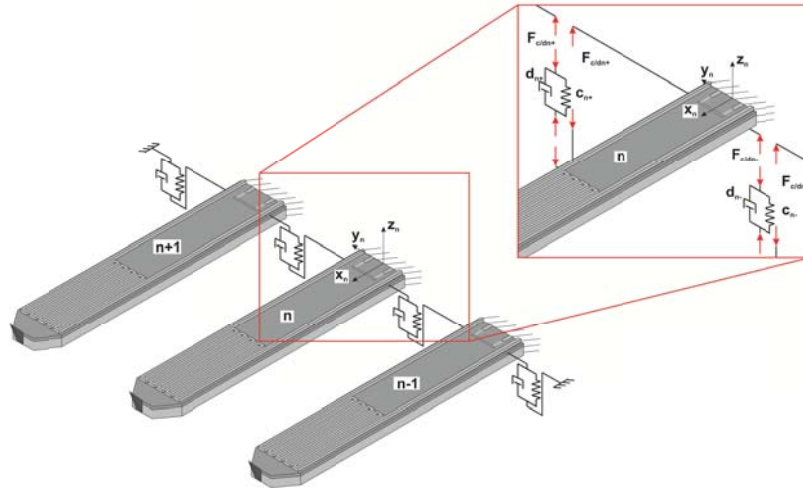


Figure 3: Schematic of an array with three microbeams and free body diagram.

elements are attached at the distance l_c measured from the clamped end. The coupling at position $\tilde{x}_n = l_c$ is described by (c.f. Figure 3)

$$F_{cdn} = (F_{cn+} - F_{cn-})\delta(\tilde{x}_n - l_c) + (F_{dn+} - F_{dn-})\delta(\tilde{x}_n - l_c), \quad (9)$$

where $\delta(\)$ is a Dirac function, $F_{cn\mp}$ are the spring forces acting between the $(n - 1)$ -th and n -th and between the n -th and the $(n + 1)$ -th beam:

$$F_{cn-} = (\tilde{w}_n - \tilde{w}_{n-1})\tilde{c}_{n-}, \quad F_{cn+} = (\tilde{w}_{n+1} - \tilde{w}_n)\tilde{c}_{n+}. \quad (10)$$

The forces corresponding to the damping elements are:

$$F_{dn-} = \frac{\partial}{\partial \tilde{t}}(\tilde{w}_n - \tilde{w}_{n-1})d_{n-}, \quad F_{dn+} = \frac{\partial}{\partial \tilde{t}}(\tilde{w}_{n+1} - \tilde{w}_n)d_{n+}. \quad (11)$$

The stiffness and damping coefficient of the base are $\tilde{c}_{n\mp}$ and $d_{n\mp}$. Note that the inter-atomic forces acting between each microbeam's tip and the sample surface $F_{TSn}(\tilde{w}_n)$ in (3) are neglected in this case.

Considering the thermal term in (3), the heat flux of the n -th element can be express by

$$Q_{HF_n}(\tilde{\theta}_n) = \frac{\overline{k_t A_n}}{c_v \rho \overline{A_n} + T_0 E_{n1} \overline{A_n} \overline{\alpha_n^2}} \frac{\partial^2}{\partial x_n^2} \tilde{\theta}_n, \quad (12)$$

where k_{tn} is the thermal conductivity and c_{vn} the specific heat capacity. The coupling and excitation term $Q_{CE_n}(\tilde{w}_n, \tilde{t})$ consists of the heat generation due to a mechanical deformation and the internal heat generation by means of Joule heating within the aluminum microactuator

$$Q_{CE_n}(\tilde{w}_n, \tilde{t}) = \frac{T_0 E_{n1} (\overline{S_{yn} A} \overline{\alpha_n A_n} - \overline{S_y \alpha_n})}{c_v \rho \overline{A_n} + T_0 E_{n1} \overline{A_n} \overline{\alpha_n^2}} \frac{\partial^3}{\partial x_n^2 \partial t} \tilde{w}_n + \frac{\overline{A_n}}{c_v \rho \overline{A_n} + T_0 E_{n1} \overline{A_n} \overline{\alpha_n^2}} g_n(\tilde{t}). \quad (13)$$

The internal heat generation $g_n(\tilde{t})$ in (13) is given by the heat dissipated within the aluminum layer due to resistive heating with respect to the volume of the meander shape aluminum layer, with

$$g_n(\tilde{t}) = \frac{\rho_{e0n} (1 + \alpha_{ne} \tilde{\theta}_n)}{A_{n3}^2} I_n(\tilde{t})^2. \quad (14)$$

In (14) ρ_{e0n} is the resistivity, α_{en} the temperature coefficient and A_{n3} the cross-sectional area of the aluminum layer. The excitation signal $I_n(\tilde{t})$ consisting of the static direct current i_{DCn} and the alternating current i_{ACn} can be described as

$$I_n(\tilde{t}) = i_{DCn} + i_{ACn} \sin \Omega_n \tilde{t}, \quad (15)$$

where Ω_n is the excitation frequency.

Introducing the following set of nondimensional variables

$$x_n = \frac{\tilde{x}_n}{L_n}, w_n = \frac{\tilde{w}_n}{H_n}, t = \omega_s \tilde{t}, \theta_n = \frac{\tilde{\theta}_n}{T_0}, \quad (16)$$

with the elastic frequency $\omega_s^2 = (\overline{I_{yn} A_n} - \overline{S_{yn}^2}) E_{n1} / (L_n^4 \mu_n \overline{A_n})$, Eq. (3) is rewritten as

$$\begin{aligned}
\frac{\partial^2}{\partial t^2} w_n = & -2D_{cln} \frac{\partial}{\partial t} w_n - \frac{\partial^4}{\partial x_n^4} w_n + \chi_{wn1} \frac{\partial^2}{\partial x_n^2} \theta_n \\
& + \chi_{wn2} (w_{n+1} - 2w_n + w_{n-1}) \delta(x - l_c/L_n) \\
& + \chi_{wn3} \frac{\partial}{\partial t} (w_{n+1} - 2w_n + w_{n-1}) \delta(x - l_c/L_n),
\end{aligned} \tag{17}$$

$$\frac{\partial}{\partial t} \theta_n = \chi_{\theta n1} \frac{\partial^2}{\partial x_n^2} \theta_n - \chi_{\theta n2} I_n^2 \theta_n - \chi_{\theta n3} \frac{\partial^3}{\partial x_n^2 \partial t} w_n + \chi_{\theta n4} I_n^2.$$

D_{cln} in (17) is the damping ratio of a microbeam. The dimensionless coefficients χ_{wn1} to χ_{wn7} of the mechanical system and the coefficients $\chi_{\theta n1}$ to $\chi_{\theta n4}$ of the thermal system can be found in Table 2 and Table 3 in Appendix A. The corresponding nondimensional boundary conditions of (17) are:

$$\begin{aligned}
w_n(0, t) = 0, \quad \frac{\partial}{\partial x_n} w_n(0, t) = 0, \\
-\chi_{wn6} \frac{\partial^2}{\partial x_n^2} w_n(1, t) + \chi_{wn7} \theta_n(1, t) = 0 \\
-\frac{\chi_{wn6}}{L_n} \frac{\partial^3}{\partial x_n^3} w_n(1, t) + \frac{\chi_{wn7}}{L_n} \frac{\partial}{\partial x_n} \theta_n(1, t) = 0 \\
\theta_n(0, t) = 0, \quad \frac{\partial}{\partial x_n} \theta_n(1, t) = 0.
\end{aligned} \tag{18}$$

2.3. Modal Dynamic Array

To analyze the dynamic response of the array, the solution of the governing equations (17) can be approximated in terms of a linear combination of a finite number of orthonormal spatial basis functions with time dependent amplitudes, which yields:

$$\begin{aligned}
w_n(x_n, t) = \sum_{k=1}^p \phi_{wnk}(x_n) q_{wnk}(t), \\
\theta_n(x_n, t) = \sum_{k=1}^p \phi_{\theta nk}(x_n) q_{\theta nk}(t),
\end{aligned} \tag{19}$$

wherein ϕ_{wnk} and $\phi_{\theta nk}$ are the mechanical and thermal spatial shape functions and q_{wnk} and $q_{\theta nk}$ are the time varying amplitudes, corresponding to the k -th mode of oscillation; p is the number of modes consider in the modal decomposition. The shape functions, which satisfy the boundary conditions exactly [27] are determined by solving the eigenvalue problem of a single beam with a springs attached at a distance l_c from the clamped end.

Introducing ansatz (19) into (17) and applying the general procedure for a modal analysis by multiplying the resulting mechanical equations with ϕ_{wnm} and the

corresponding thermal equations with $\phi_{\theta nm}$ as well as integrate with respect to x_n yields:

$$\begin{aligned} J_{wn1}\ddot{q}_{wn} = & -2(D_{cln}J_{wn1} + \chi_{wn3}\widehat{\phi}_{wn}^2)\dot{q}_{wn} - (J_{wn2} + 2\chi_{wn2}\widehat{\phi}_{wn}^2)q_{wn} \\ & + \chi_{wn1}J_{wn3}q_{\theta n} + \phi_{wn}\phi_{wn+1}^T(\chi_{wn3}\dot{q}_{wn+1} + \chi_{wn2}q_{wn+1}) \\ & + \phi_{wn}\phi_{wn-1}^T(\chi_{wn3}\dot{q}_{wn-1} + \chi_{wn2}q_{wn-1}) \end{aligned} \quad (20)$$

$$J_{\theta n1}\dot{q}_{\theta n} = (\chi_{\theta n1}J_{\theta n2} - \chi_{\theta n2}I_n^2J_{\theta n1})q_{\theta n} - \chi_{\theta n3}J_{\theta n3}\dot{q}_{wn} + \chi_{\theta n4}I_n^2J_{\theta n4}$$

with $\widehat{\phi}_{wn} = \phi_{wn}(l_c/L_n)$. Note that dot ($\dot{\quad}$) and prime (\prime) denote ordinary derivatives with respect to the nondimensional time t and coordinate x_n along the beams length. The matrices J_{wn1} to J_{wn3} and $J_{\theta n1}$ to $J_{\theta n3}$ contain the inner product of the mechanical and thermal eigenfunctions (see Appendix A, Table 4).

Introducing the following state vector

$$X = [q_{w1}^T \quad \cdots \quad q_{wn}^T \quad \cdots \quad q_{wN}^T \quad \dot{q}_{w1}^T \quad \cdots \quad \dot{q}_{wn}^T \quad \cdots \quad \dot{q}_{wN}^T]^T, \quad (21)$$

and assuming that $q_{w0} = 0$, $q_{wh} = 0$; $\dot{q}_{w0} = 0$ and $\dot{q}_{wh} = 0$, (20) can be written in state space to:

$$\dot{X} = \begin{bmatrix} \mathbf{0}_h & I_h \\ K_h & D_h \end{bmatrix} X + Q_{ex}, \quad (22)$$

with $\mathbf{0}_n$ and I_n being a zero matrix and an identity matrix, respectively. The stiffness and damping matrix K_h and D_h can be found in the Appendix A, Table 5.

Note that in case of (22) the bidirectional coupling of the thermal and mechanical system of a single element is neglected. Thus, the systems excitation is:

$$Q_{ex} = \chi_{w3}J_{wn3}q_{\theta} \quad (23)$$

where the vector q_{θ} consists of the time dependent amplitudes of each beam $q_{\theta nk}$.

3. ANALYSIS

The analysis carried out within the following sections is divided into two parts: The analysis of the analytical model with the corresponding eigenvalue problem and a modal analysis of a finite element (FE) model. Conclusively, both models are compared in view of a qualitative agreement and to evaluate the limits of the analytical array model.

3.1 Analysis of Eigenvalue Problem

The eigenvalue problem of the governing equation of motion (20) is analyzed in view of eigenfrequencies and coupled modes of the 4 element array and the dependency of these properties on the geometry of the common base. In case of the analytical model, the nondimensional coefficients χ_{wn2} and χ_{wn3} , are the equivalent coefficients to the base geometry and correspond to a stiffness and damping coefficient of the coupling element. Additionally, the position of the coupling elements l_c along the beam's x_n axis can be varied. The coupled modes of the array are denoted in the following manner (Fig. 4):

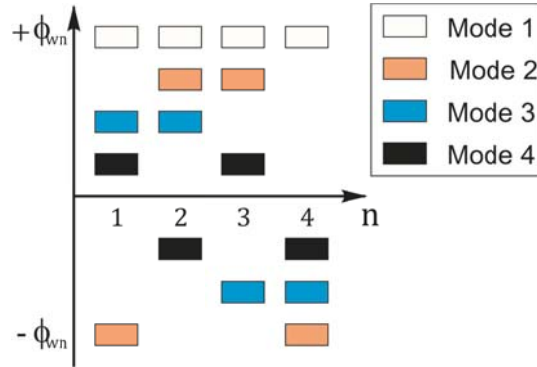


Figure 4: Coupled assembly modes 1 to 4 of the 4 element microbeam array.

For instance, the third mode follows a pattern, in which the elements $n = 1$ and $n = 2$ are in phase whereas beams $n = 3$ and $n = 4$ oppose them. Note that the position of the mode markers does not correspond to the amplitude of the mode.

In a trivial configuration, wherein either the distance l_c or the spring and damper constant of the coupling elements are identical zero, only the four intrinsic modes of the individual beams can be observed, with no coupling. On the other hand, large values for the nondimensional stiffness coefficient c_n will also lead to an uncoupled behavior. In case of a varying c_n in the range of $[10^{-2}, 10^{10}]$ and a variation of $\kappa = l_c/L_n$ within $[0.1, 0.8]$, the ratio of the n -th beam's eigenfrequency to the eigenfrequency of a single microbeam with clamped free boundary conditions can be seen in Fig. 5.

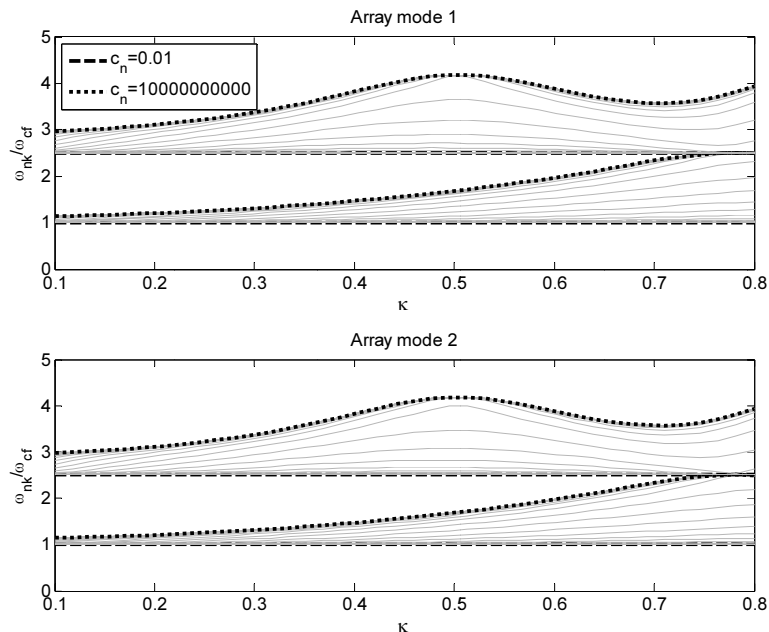


Figure 5: Variation of the eigenfrequency ratio for the 1st and 2nd array mode with respect to the stiffness coefficient c_n and the dimensionless distance between spring and clamped end of the beam κ .

Both graphs in Fig. 5 show the change of frequencies of the 1st and 2nd intrinsic mode over κ . The frequency ratios at $\kappa = 0.1$ are $\omega_{n1}/\omega_{cf} = 1$ and $\omega_{n1}/\omega_{cf} \approx 2.5$, respectively. Both of these ratios are also illustrated in Fig. 5. In case of an increasing

stiffness c_n , the first and second intrinsic modes occur at the same frequency. This is due to the location of the coupling element, which is located near the node of the second eigenfrequency. In case of small κ , an increasing stiffness c_n leads to an increasing difference between the 1st and 2nd intrinsic mode of each microbeam.

The first assembly mode for $l_c = 0.2$ and $c_n = 10^5$ is depicted in Fig. 6. As can be seen, two pairs of members are forming between the 1st and 4th element as well as between the 2nd and 3rd element. These different amplitudes of oscillation result from the different boundary condition in the y_n coordinate. The outer beams are connected to only one neighboring element and to a fixed support, whereas the beams in the middle of the array connected with 2 neighboring elements.

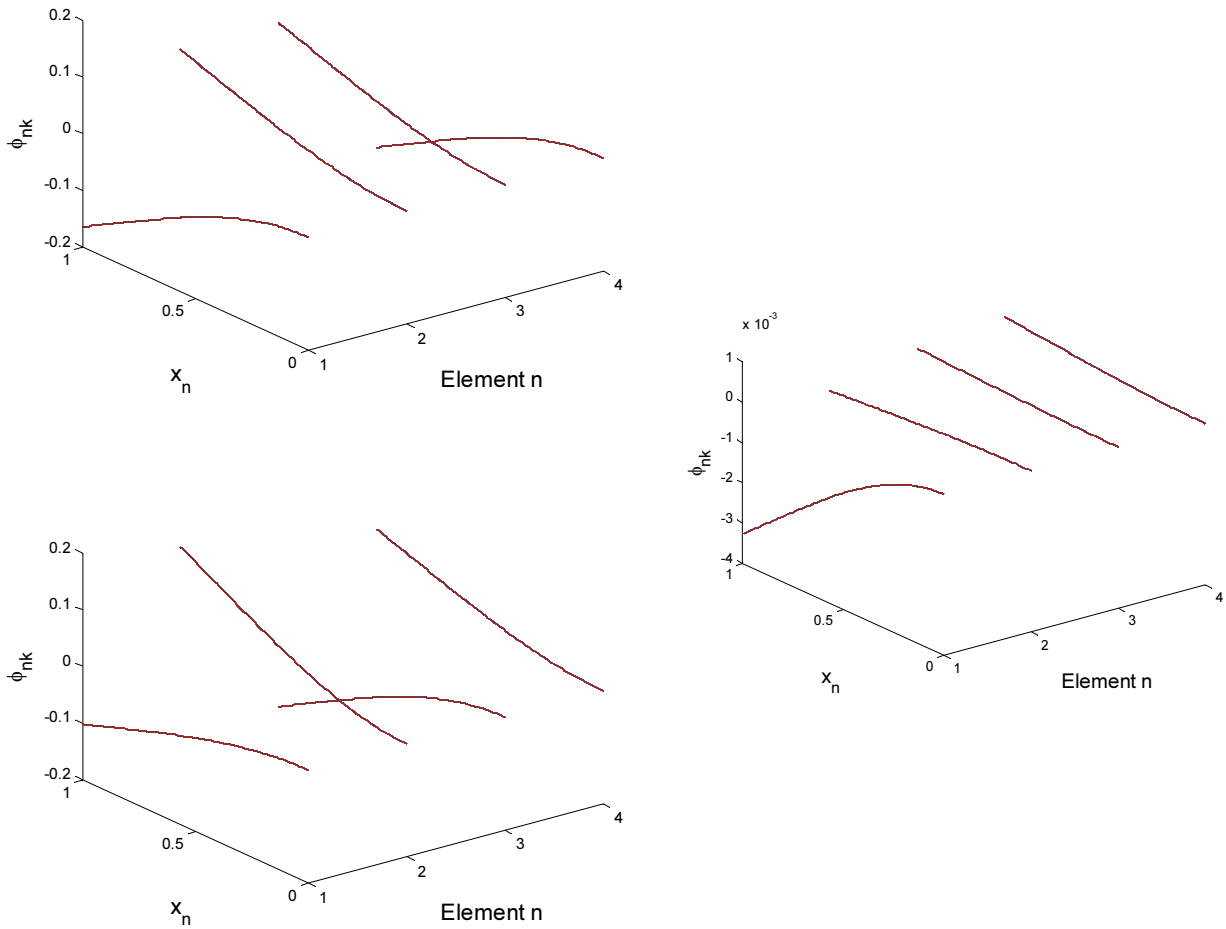


Figure 6: Left: 4th and 2nd coupled mode of the array; $c_n = 10^5$, $l_c = 0.2$. Right: Decoupled mode for $\kappa \rightarrow 0$ or $c_n \rightarrow 0$ or $c_n \rightarrow \infty$.

3.2 Modal Analysis Finite Element Model

The modal analysis of a finite element (FE) array model is done using ANSYS Workbench v14. The geometry of each single microbeam is similar to the parameters

used in the analysis of the eigenvalue problem of the analytical model in the foregone section. The FE model also includes the base all microbeams share, with the dimensions l_c , h_b and $B_{cln\bar{\tau}}$ (see Section 2.1), which, in turn, yield the stiffness of the base. The mesh is generated using hexahedral elements with size functions depending on the thickness of each layer, so that at least one elements fits the thickness if the aluminum and silicon dioxide layer. The array is built from cells of a single microbeam with its base (see Fig. 7).

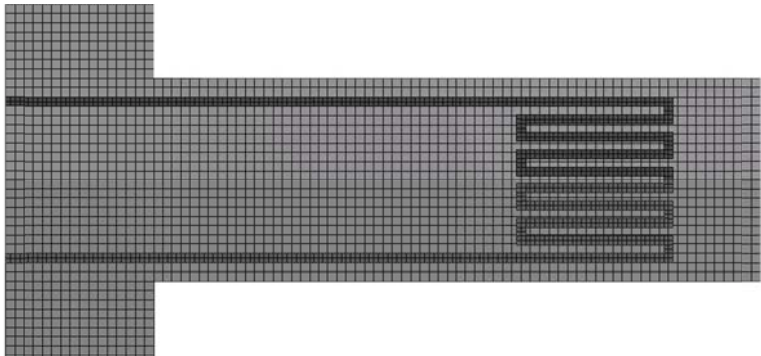


Figure 7: Ansys mesh and single cell for FE simulations.

Similar to the results gained from the analysis of the analytical model in Section 2.3, the FE model yields an uncoupled behavior of members in the case of a high rigidity of the common base, see Fig. 8.

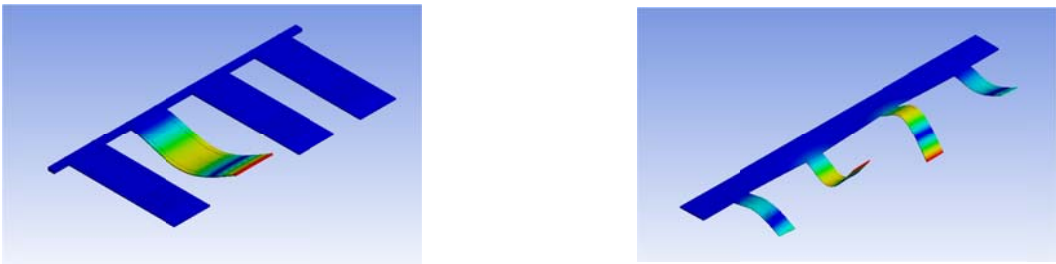


Figure 8: Uncoupled mode of the second microbeam (left; $l_c = 20 \mu m$, $h_b = 5 \mu m$, $B_{cln\bar{\tau}} = 80 \mu m$) and coupled behavior in the 4th array mode (right; $l_c = 160 \mu m$, $h_b = 5 \mu m$, $B_{cln\bar{\tau}} = 400 \mu m$) for different geometrical parameters of the base.

Depending on the geometry of the array’s base, there might be a superposition of bending and torsional modes or occurrence of plate modes. As can be seen in Fig. 9, the eigenmodes change from individual, pure bending and torsional modes to the modes of a plate with increasing the length of the base. In this case of weak coupling, the system’s behavior can no longer be described accurately by means of an Euler-Bernoulli beam model. Due to the superposition of torsional and bending modes a plate model is needed in order to describe the systems motion.

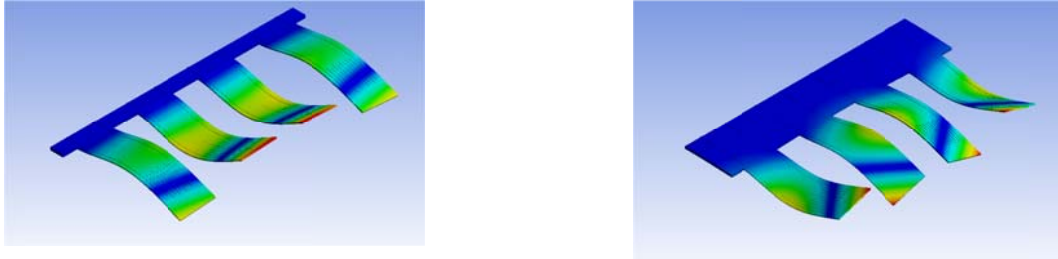


Figure 9: Superposition of a bending and torsional mode at the second intrinsic bending (left, $l_c = 40 \mu m$, $h_b = 5 \mu m$, $B_{cln\bar{\tau}} = 80 \mu m$) and a plate mode in case a large thin base (right; $l_c = 160 \mu m$, $h_b = 5 \mu m$, $B_{cln\bar{\tau}} = 80 \mu m$)

The findings of the analytical model are qualitatively validated by the FE analysis. While the coupling mechanism can be successively modeled by discrete spring and damping elements, the analytical model of an individual member should be modeled as a plate structure when coupling is expected. A performance of a micro cantilever array which is dominated by coupled torsional and bending motion cannot be successfully predicted using the simplified Euler-Bernoulli beam theory.

4. CONCLUSIONS

In summary, a first dynamical model is presented, which captures the behavior of an array of thermally actuated microbeams. The model incorporates the composite structure of a single beam and takes account for the physical effect of thermal actuation. It also captures the thermoelastic interactions, which result in a damping of the system, which especially in case of small beams becomes of importance. The equations of motion are coupled by means of discrete spring and damping elements, representing the common base of an array.

A modal analysis of the analytical model and a FE model was carried out with respect the geometrical parameters of the base or clamped boundary of the beam. The coupling via discrete coupling elements yields a sufficient approximation of the systems behavior in case of a high stiffness coefficient of the base. In case of a lower stiffness ratio between the microbeam and the base, only the first bending modes of the array can be approximated.

Our future work will be related to different sets of boundary conditions and varying beam models in order to gain a good approximation of the vibration of an array. The boundary conditions are going to be validated experimentally. To evaluate the coupled behavior in case of a low stiffness and low aspect ratio base, a thermoelastic plate model is going to be derived to capture the coupled bending and torsional modes of the single elements of an array.

Acknowledgment

This work is supported by the Carl Zeiss Foundation, for which we express our gratefulness.

APPENDIX A

Table 1: Weighted material parameters and moments of area

$n_n = \frac{E_{ni}}{E_{n1}}$	$\bar{A}_n = \sum_i n_{ni} A_{ni}$	$\bar{S}_{yn} = \sum_i n_{ni} S_{yni}$	$\bar{A}\bar{\alpha}_n = \sum_i n_{ni} \alpha_{ni} A_{ni}$
$\bar{k}_t \bar{A}_n = \sum_i k_{tni} A_{ni}$	$\bar{c}_v \bar{\rho} \bar{A}_n = \sum_i c_{vni} \rho_{ni} A_{ni}$	$S_{yni} = \int_{(A_n)} dA_n$	$I_{yni} = \int_{(A_n)} z_n dA_n$

Table 2: Coefficients of the mechanical system

$\chi_{wn1} = (\bar{A} \bar{\alpha}_n \bar{S}_{yn} - \bar{A}_n \bar{S}_y \bar{\alpha}_n) \frac{E_1 T_0}{\bar{A}_n \mu_n \omega_{sn}^2 H_n L_n^2}$	$\chi_{wn2} = \frac{E_{n1} I_{yn} c_n}{\mu_n \omega_{sn}^2 L_n^3}$
$\chi_{wn3} = 2D_b$	$\chi_{wn4} = \frac{A_1 R_{tn}}{6 \omega_{sn}^2 H_n \mu_n \xi_{0n}^2}$
$\chi_{wn5} = \frac{A_2 R_{tn}}{180 \omega_{sn}^2 H_n \mu_n \xi_{0n}^8}$	$\chi_{wn6} = (\bar{A}_n \bar{I}_{yn} - \bar{S}_{yn}^2) \frac{E_{n1} H_n}{\bar{A}_n L_n^2}$
$\chi_{wn7} = (\bar{A} \bar{\alpha}_n \bar{S}_{yn} - \bar{A}_n \bar{S}_y \bar{\alpha}_n) \frac{E_{n1} T_0}{\bar{A}_n}$	$D_{cl} = \frac{d_p}{2 \mu_n \omega_{sn}}$

Table 3: Coefficients of the thermal system

$\chi_{\theta n1} = \frac{\bar{k}_t \bar{A}_n}{(\bar{c}_v \bar{\rho} \bar{A}_n + T_0 E_{n1} \bar{A} \bar{\alpha}_n^2 \bar{A}_n) L_n^2 \omega_{sn}}$	$\chi_{\theta n2} = \frac{A_n \alpha_e \rho_{e0} \sum_i A_n}{(\bar{c}_v \bar{\rho} \bar{A}_n + T_0 E_{n1} \bar{A} \bar{\alpha}_n^2 \bar{A}_n) \omega_{sn} A_{3n}^2}$
$\chi_{\theta n3} = \frac{E_{n1} (\bar{S}_{yn} \bar{A} \bar{\alpha}_n \bar{A}_n^{-1} - \bar{S}_y \bar{\alpha}_n)}{(\bar{c}_v \bar{\rho} \bar{A}_n + T_0 E_{n1} \bar{A} \bar{\alpha}_n^2 \bar{A}_n) L_n^2 \omega_{sn}}$	$\chi_{\theta n4} = \frac{\rho_{e0} A_n \sum_i A_n}{T_0 \omega_{sn} A_{n3}^2 (\bar{c}_v \bar{\rho} \bar{A}_n + T_0 E_{n1} \bar{A} \bar{\alpha}_n^2 \bar{A}_n)}$

Table 4: Matrices of the inner product of the mechanical and thermal eigenfunctions

$J_{wn1} = \begin{bmatrix} \int_0^1 \phi_{wn1}^2 dx & \cdots & 0 \\ \vdots & \ddots & \vdots \\ 0 & \cdots & \int_0^1 \phi_{wnp}^2 dx \end{bmatrix}$	$J_{wn2} = \begin{bmatrix} \int_0^1 \phi_{wn1} \phi_{\theta n1}''''^T dx & \cdots & \int_0^1 \phi_{wn1} \phi_{\theta np}''''^T dx \\ \vdots & \ddots & \vdots \\ \int_0^1 \phi_{wnp} \phi_{\theta n1}''''^T dx & \cdots & \int_0^1 \phi_{wnp} \phi_{\theta np}''''^T dx \end{bmatrix}$
$J_{wn3} = \begin{bmatrix} \int_0^1 \phi_{wn1} \phi_{\theta n1}''^T dx & \cdots & \int_0^1 \phi_{wn1} \phi_{\theta np}''^T dx \\ \vdots & \ddots & \vdots \\ \int_0^1 \phi_{wnp} \phi_{\theta n1}''^T dx & \cdots & \int_0^1 \phi_{wnp} \phi_{\theta np}''^T dx \end{bmatrix}$	$J_{\theta n1} = \begin{bmatrix} \int_0^1 \phi_{\theta n1}^2 dx & \cdots & 0 \\ \vdots & \ddots & \vdots \\ 0 & \cdots & \int_0^1 \phi_{\theta np}^2 dx \end{bmatrix}$
$J_{\theta n2} = \begin{bmatrix} \int_0^1 \phi_{\theta n1} \phi_{wn1}''^T dx & \cdots & 0 \\ \vdots & \ddots & \vdots \\ 0 & \cdots & \int_0^1 \phi_{wnp} \phi_{\theta np}''^T dx \end{bmatrix}$	$J_{\theta n3} = \begin{bmatrix} \int_0^1 \phi_{\theta n1} \phi_{wn1}''^T dx & \cdots & \int_0^1 \phi_{\theta n1} \phi_{wnp}''^T dx \\ \vdots & \ddots & \vdots \\ \int_0^1 \phi_{\theta np} \phi_{wn1}''^T dx & \cdots & \int_0^1 \phi_{\theta np} \phi_{wnp}''^T dx \end{bmatrix}$

Table 5: Nondimensional stiffness and damping matrices and coefficients

$K_h = \begin{bmatrix} C_{21} & C_{31} & & & & \dots & & & \mathbf{0}_o \\ C_{12} & C_{22} & C_{32} & & & & & & \vdots \\ & & \ddots & \ddots & & & & & \\ & & & C_{1n} & C_{2n} & C_{3n} & & & \\ \vdots & & & & \ddots & \ddots & \ddots & & \\ \mathbf{0}_u & \dots & & & & C_{1h-1} & C_{2h-1} & C_{3h-1} \\ & & & & & & C_{2h} & C_{3h} \end{bmatrix}$		
$D_h = \begin{bmatrix} D_{21} & D_{31} & & & & \dots & & & \mathbf{0}_o \\ D_{12} & D_{22} & D_{32} & & & & & & \vdots \\ & & \ddots & \ddots & & & & & \\ & & & D_{1n} & D_{2n} & D_{3n} & & & \\ \vdots & & & & \ddots & \ddots & \ddots & & \\ \mathbf{0}_u & \dots & & & & D_{1h-1} & D_{2h-1} & D_{3h-1} \\ & & & & & & D_{2h} & D_{3h} \end{bmatrix}$		
$C_{1n} = J_{w1}^{-1} \widehat{\phi}_{wn} \widehat{\phi}_{wn-1}^T \chi_{w2}$	$C_{2n} = -J_{w1}^{-1} (J_{w2} + 2 \chi_{w2} \widehat{\phi}_{wn}^2);$	$C_{3n} = J_{w1}^{-1} \widehat{\phi}_{wn} \widehat{\phi}_{wn+1}^T \chi_{w2}$
$D_{1n} = J_{w1}^{-1} \widehat{\phi}_{wn} \widehat{\phi}_{wn-1}^T \chi_{w3}$	$D_{2n} = -2(D I_n + \chi_{w3} J_{w1}^{-1} \widehat{\phi}_{wn}^2);$	$D_{3n} = J_{w1}^{-1} \widehat{\phi}_{wn} \widehat{\phi}_{wn+1}^T \chi_{w3}$

Table 6 Parameters

Parameter		Unit	Symbol	Value
Height	Layer 1	μm	h_i	3
	Layer 2			0.6
	Layer 3			1
Length	Section 1	μm	l_j	203
	Section 2			77
	Section 3			40
Width		μm	B	111
Tip Radii		nm	R_t	20
Tip height		μm	h_T	10
Tip to beam end distance		μm	l_T	10
Length piezoresistive element		μm	l_{PE}	28
Width piezoresistive element		μm	b_{PE}	6
Position piezoresistive sensor (midelle)		μm	l_{PS}	10
Heater length		mm	l_h	1.18
Heater width	Section 1	μm	b_{Hj}	3
	Section 2			4.5
Distance between each cantilever		μm	d_{CLnm}	60
Length of base (clamp)		μm	l_B	
Height of base (clamp)		μm	h_B	
Young's modulus	Layer 1	GNm^2	E_i	170
	Layer 2			74
	Layer 3			70
Density	Layer 1	kgm^{-3}	ρ_i	2300
	Layer 2			2210
	Layer 3			2694
Poisson's ratio	Layer 1	1	ν_i	0.22
	Layer 2			0.17
	Layer 3			0.35
Coefficient of linear thermal expansion	Layer 1	10^{-6}K^{-1}	α_{Ti}	2.616
	Layer 2			0.54
	Layer 3			23.3
Thermal conductivity	Layer 1	W (m K)^{-1}	k_t	156
	Layer 2			1.4
	Layer 3			237
Specific heat capacity	Layer 1	J (kg K)^{-1}	c_v	713
	Layer 2			705
	Layer 3			753
Quality Factor		1	Q	516.13
Resistivity (layer 3 aluminum)		$10^{-8} \Omega \text{ m}$	ρ_e	2.857
Heater resistance		Ω	R_h	24
Sensor resistance		Ω	R_s	1090
Hamaker constant	repulsive	10^{-70}J m^6	H_1	1.3596
	attractive	10^{-19}J	H_2	1.865

REFERENCES

1. Giessibl, F.J., *Advances in atomic force microscopy*. Reviews of Modern Physics, 2003. **75**(3): p. 949-983.
2. Wiesendanger, R., *Contributions of Scanning Probe Microscopy and Spectroscopy to the Investigation and Fabrication of Nanometer-Scale Structures*. Journal of Vacuum Science & Technology B, 1994. **12**(2): p. 515-529.
3. Wiesendanger, R., *Scanning Probe Microscopy and Spectroscopy*. 1994: Cambridge University Press.
4. Minne S. C., M.S.R., Quate Calvin F. , *Bringing Scanning Probe Microscopy Up to Speed* Microsystems. Vol. 3. 1999: Kluwer Academic Publishers.
5. *PRONANO: Proceedings of the Integrated Project on Massively Parallel Intelligent Cantilever Probe Platforms for Nanoscale Analysis and Synthesis*, ed. T.a.R. Sulzbach, I.W. (Eds.). 2010: Verlagshaus Monsenstein und Vannerdat OHG Münster.
6. Ivanova, K., et al., *Scanning proximal probes for parallel imaging and lithography*. Journal of Vacuum Science & Technology B, 2008. **26**(6): p. 2367-2373.
7. Rangelow, I.W., *Piezoresistive scanning proximity probes for nanoscience*. Tm-Technisches Messen, 2005. **72**(2): p. 103-110.
8. Sattel, T.a.R., D. and Gutschmidt, S. *Multi-physics modeling of an electrothermally actuated micro-cantilever for scanning probe microscopy*. in *ASME 2010 International Mechanical Engineering Congress and Exposition*. 2010. Vancouver, Canada.
9. Bennett, M., et al., *Huygens's clocks*. Proceedings of the Royal Society of London Series a-Mathematical Physical and Engineering Sciences, 2002. **458**(2019): p. 563-579.
10. Dick, A.J., B. Balachandran, and C.D. Mote, *Intrinsic localized modes in microresonator arrays and their relationship to nonlinear vibration modes*. Nonlinear Dynamics, 2008. **54**(1-2): p. 13-29.
11. Gutschmidt, S. and O. Gottlieb, *Nonlinear dynamic behavior of a microbeam array subject to parametric actuation at low, medium and large DC-voltages*. Nonlinear Dynamics, 2012. **67**(1): p. 1-36.
12. Kenig, E., et al., *Intrinsic localized modes in parametrically driven arrays of nonlinear resonators*. Physical Review E, 2009. **80**(4).
13. Younis, M.I., E.M. Abdel-Rahman, and A. Nayfeh, *A reduced-order model for electrically actuated microbeam-based MEMS*. Journal of Microelectromechanical Systems, 2003. **12**(5): p. 672-680.
14. Bromberg, Y., M.C. Cross, and R. Lifshitz, *Response of discrete nonlinear systems with many degrees of freedom*. Physical Review E, 2006. **73**(1).
15. Kenig, E., R. Lifshitz, and M.C. Cross, *Pattern selection in parametrically driven arrays of nonlinear resonators*. Physical Review E, 2009. **79**(2).
16. Nayfeh, A.H., M.I. Younis, and E.M. Abdel-Rahman, *Reduced-order models for MEMS applications*. Nonlinear Dynamics, 2005. **41**(1-3): p. 211-236.
17. Nayfeh, A.H., M.I. Younis, and E.M. Abdel-Rahman, *Dynamic analysis of MEMS resonators under primary-resonance excitation*. Proceedings of the ASME International Design Engineering Technical Conferences and Computers and Information in Engineering Conference, Vol 1, Pts A-C, 2005: p. 397-404.
18. Younis, M.I., E.M. Abdel-Rahman, and A.H. Nayfeh, *Global dynamics of MEMS resonators under superharmonic excitation*. 2004 International Conference on Mems, Nano and Smart Systems, Proceedings, 2004: p. 694-699.

19. Krylov, S., *Lyapunov exponents as a criterion for the dynamic pull-in instability of electrostatically actuated microstructures*. International Journal of Non-Linear Mechanics, 2007. **42**(4): p. 626-642.
20. Nayfeh, A.H., M.I. Younis, and E.M. Abdel-Rahman, *Dynamic pull-in phenomenon in MEMS resonators*. Nonlinear Dynamics, 2007. **48**(1-2): p. 153-163.
21. Younis, M.I. and A.H. Nayfeh, *A study of the nonlinear response of a resonant microbeam to an electric actuation*. Nonlinear Dynamics, 2003. **31**(1): p. 91-117.
22. Gottlieb, O. and A.R. Champneys, *Global bifurcations of nonlinear thermoelastic microbeams subject to electrodynamic actuation*. IUTAM Symposium on Chaotic Dynamics and Control of Systems and Processes in Mechanics, 2005. **122**: p. 117-126.
23. Wolf, K. and O. Gottlieb, *Nonlinear dynamics of a noncontacting atomic force microscope cantilever actuated by a piezoelectric layer*. Journal of Applied Physics, 2002. **91**(7): p. 4701-4709.
24. Nowinski, J.L., *Theory of thermoelasticity with applications*. 1978, Alphen aan den Rijn: Sijthoff & Noordhoff International Publishers.
25. Arafat, H.N., A.H. Nayfeh, and E.M. Abdel-Rahman, *Modal interactions in contact-mode atomic force microscopes*. Nonlinear Dynamics, 2008. **54**(1-2): p. 151-166.
26. Watanabe, N.a.I., Y. and Kakinaga, T. and Nagamura, T. and Sasaki, T., *Thermal actuated multi-probes cantilever array for scanning probe parallel nano writing system*, in *Micro Electro Mechanical Systems, 2007. MEMS. IEEE 20th International Conference on*. 2007. p. 99-102.
27. Hagedorn, P.a.D., A. , *Vibrations and Waves in Continuous Mechanical Systems*. 2007, Chichester: Wiley.